Doping change in the Bi-2212 superconductor directly induced by a hard X-ray nano-beam

Doping change in the Bi-2212 superconductor directly induced by a hard X-ray nano-beam

Alessandro Pagliero[§], Lorenzo Mino[‖], Elisa Borfecchia[‖], Marco Truccato[,§], Angelo Agostino[‖,#], Lise Pascale[‖], Emanuele Enrico[†], Natascia De Leo[†], Carlo Lamberti[‖,#,‡], Gema Martínez-Criado[⊥]*

[§] Dept. of Physics and Interdepartmental Centre NIS, University of Torino, via Giuria 1, I-10125 Torino, Italy

[‖] Dept. of Chemistry, University of Torino, via Giuria 7, I-10125 Torino, Italy; Interdepartmental Centre NIS and INSTM Centro di Riferimento via Quarello 11, I-10135 Torino, Italy

[#] CrisDi Interdepartmental Center for Crystallography, University of Torino, Italy

[‡]Southern Federal University, Zorge street 5, 344090 Rostov-on-Don, Russia

[†]INRIM, National Institute of Metrological Research, Strada delle Cacce 91, I-10135 Torino, Italy

[⊥] Experiments Division, European Synchrotron Radiation Facility, 6, rue Jules Horowitz, B.P. 220, F-38043 Grenoble Cedex, France

*****Corresponding author: marco.truccato@unito.it

Keywords: High-Temperature Superconductors (HTSC), Bi-2212, single crystal, doping, nano-lithography, X-rays nano-beam, whiskers

ABSTRACT

We describe the controlled use of a 17 keV X-ray synchrotron nano-beam to progressively change the oxygen doping level in Bi-2212 superconducting whisker-like single crystals. Our data combine structural and electrical information collected on the same crystals, showing a maximum change in the critical temperature T_c of 1.3 K and a maximum elongation of about 1 Å in the *c*-axis length, compared to the as-grown conditions. Simulations of our experimental conditions by means of a finite element model exclude local heating induced by the X-ray nano-beam as a possible cause for the change in the doping level and suggest an important role of secondary electrons. These findings support the possible use of hard X-rays as a novel direct-writing, photoresist-free lithographic process for the fabrication of superconducting devices, with potential nanometric resolution and 3D capability.

In the past few decades, the goal of achieving higher speed and lower power consumption has driven the semiconductor industry to design and produce smaller and smaller integrated circuits. This trend has stimulated deep innovation in the lithographic techniques, setting for instance the 193-nm immersion technology as the present standard for the 32-nm node.[1] However, further decrease in half-pitch size down to 22 nm has been made possible thanks to the development of a technique based on Extreme Ultra Violet (EUV) radiation with much shorter wavelength (λ =13.5 nm), which in its pre-production implementations was provided by synchrotron radiation facilities.[2,3] Nevertheless, the run towards the use of ever shorter radiation for integrated circuits

has come to a pause, since the development of lithographic processes exploiting hard X-rays with $\lambda \approx 0.1$ nm has been hindered by problems related to the fabrication of suitable masks with both high enough contrast in their absorbing power and small enough features.[1] Although some improvements have been suggested via the demagnification effect induced by near-field Fresnel diffraction,[4] it is in the field of micro-electrical-mechanical systems (MEMS) that hard X-ray lithography has shown its full potential with the introduction of the so-called LIGA process.[5,6]

All of the above-mentioned techniques are based on photo-induced chemical modifications of the photoresist layers covering the substrates, which imply the subsequent introduction of both a development and an etching stage in the fabrication process. In parallel, some direct-writing techniques have been developed to modify substrate properties without photoresists. Among them, the focused-electron-beam-[7] and the focused-ion-beam-induced deposition and etching,[8] along with the scanning-probe lithography,[9] are the most well-known; all of these techniques enable nanometric spatial resolution. Concerning X-ray direct-writing lithography, a few examples have been recently reported.[10-14] Although the use of synchrotron radiation nanoprobes has allowed spatial resolutions down to about 25 nm,[4] in all previous cases patterning was limited to organic or organometallic materials. Since these processes are essentially based on molecular photodissociation, the limitation to this kind of materials seems to be intrinsic to the use of X-rays, so that direct-writing X-ray lithography without photoresist seems impossible.

Nevertheless, from this point of view, a few experiments have shown that synchrotron radiation can directly modify the properties of inorganic materials by means of photon-induced displacement of light atoms in their crystal structure. Concerning the optical properties, it has been proved that a 100-nm beam of 640 eV photons is able to create clusters of color centers in LiF with typical sizes of about 500 nm via the production of fluorine vacancies.[15] Another

experiment has shown that a 100-μm beam at 12.4 keV is able to induce persistent changes in the transition temperature T_c of the La_2CuO_{4+y} cuprate superconductor, typically of the order of 40 K.[16] Thanks to the high oxygen mobility in this material, the X-ray radiation induces interstitial oxygen atoms to gather in more extended ordered regions, basically triggering a disorder-to-order transition that can be reversed by heating the material above 350 K. It has been proposed that this method could give rise to a future nanolithography with minimum possible resolution of about 6 nm,[16] and the present work is intended to explore this possibility for the case of superconducting oxides with T_c of more practical use such as $Bi_2Sr_2CaCu_2O_{8+\delta}$ (Bi-2212), which has typical $T_c \approx$ 80-90 K. As Bi-2212 crystals below T_c are able to emit and sense THz radiation,[17-19] an obvious application of such a technology could be represented by the production of these devices at the nanoscale. The possibility of direct-writing X-ray lithography is even more interesting because of the expected increasing availability of hard X-ray sources with very high brilliance and power, due to the development of X-ray Free Electron Lasers (XFELs). Here we investigate the effect of localized hard X-ray irradiation on Bi-2212 monitoring its influence on the structural and on the electrical properties, both in the normal and in the superconducting state. Our results can also be useful for applications of Bi-2212 in harsh radiation environments (e.g. aerospace technologies) in order to assess the shielding level required to preserve material performances.

Bi-2212 crystals with a whisker shape were selected for the purpose of this experiment because of its geometrical and defect constraints. This kind of crystals has the shape of a box with its edges aligned along the *a*-, *b*-, and *c*- axes with typical 1000:10:1 ratios in their lengths, respectively. They represent the best candidates to perform crystal structure studies under

irradiation because of their nearly perfect single-crystal nature in the pristine state, being free of macroscopic defects.[20]

These Bi-2212 whisker-like crystals were grown in controlled temperature and pressure conditions to ensure a nearly optimally-doped or slightly over-doped oxygen state.[21] After growing, they were selected under an optical microscope and mounted onto sapphire substrates with their *c*-axis parallel to the substrate plane. Four silver metallic stripes 2.5 μm thick were deposited by physical vapour deposition and provided electrical contact to the crystals after annealing at 450 °C for 5 min in O_2 gas flow. In this way, electrical measurements of the crystals were possible along the *a*-axis while allowing direct access to the X-ray beam normal to both the *ab* and *ac* crystal planes. Sizes of the two crystals analyzed in the present study are 701 x 13.55 x 1.59 μm^3 (sample WBAP013) and 750 x 4.88 x 1.59 μm^3 (sample WBAP014), respectively. Figure 1a shows the typical layout of our samples.

Electrical characterization was performed via a standard four-probe method in a continuous flow Janis ST-100 helium cryostat with I = 1 μA in the temperature range 65 K ≤ T ≤ 290 K. Irradiation and structural characterization were performed at the EH2 experimental hutch of ID22 beamline at the European Synchrotron Radiation Facility (ESRF), Grenoble, France (Figure 1b). The beamsize was 117 (vertical) x 116 (horizontal) nm^2, with an incoming photon flux at the sample position $\Phi_0 = 1.9 \times 10^{11}$ s^{-1} at the energy $E_0 = (17.054 \pm 0.004)$ keV, as determined from the elastic peak of the X-ray fluorescence spectra.

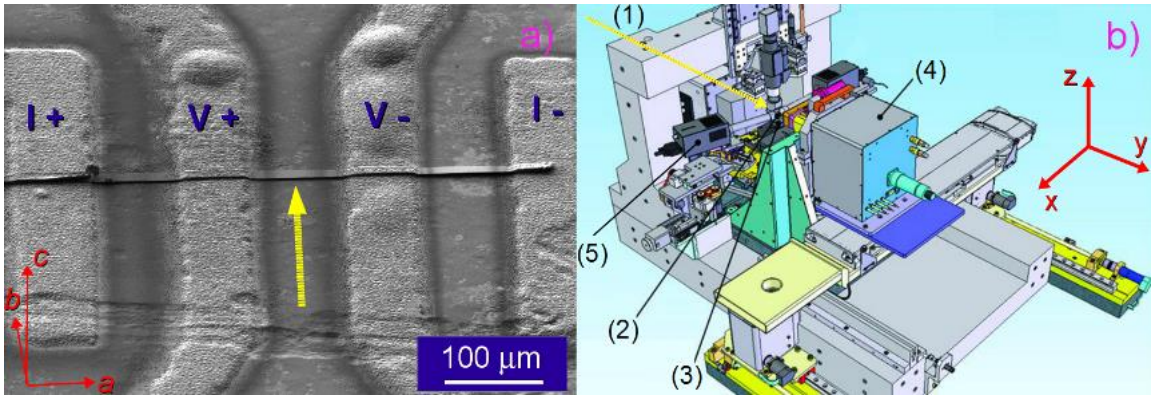

Figure 1. a) Scanning Electron Microscope (SEM) micrograph of a typical device investigated in our measurements (sample WBAP013). The current and voltage electrodes used for the four-probe technique are labeled as I+, I-, V+ and V-, respectively. The yellow arrow is representative of the grazing incidence condition with the nano-beam along the [0 1 0] direction hitting the crystal between the voltage contacts. b) Perspective view of the experimental set-up used at the ID22 beamline of ESRF to acquire both XRD frames and XRF spectra. (1) incoming X-ray nano-beam, (2) sample holder, (3) rotation stage around the *z*-axis of the laboratory frame of reference, (4) CCD diffraction camera (taper version of the ESRF FReLoN detector), and (5) energy dispersive 50 mm^2 Si drift XRF detector (Vortex-EX, SII NanoTechnology).

To assess the effect of X-rays on Bi-2212, irradiation sessions consisting in the acquisition of X-ray fluorescence (XRF) maps were alternated with X-ray diffraction (XRD) acquisitions and complementary electrical measurements performed off-line. XRF maps extended over a region of about 30 µm along the *a*-axis that was placed between the two voltage contacts, i.e. in the portion of the samples sensed by the four-probe measurement technique. The investigation started from samples in their pristine conditions; thereafter the first XRF map was collected for each sample in frontal geometry, i.e. with the beam along the [0 0 1] direction. For the

subsequent XRF maps a grazing incidence geometry with the beam parallel to the [0 1 0] direction was adopted because of its larger efficiency in energy deposition.

Acquisition of XRF data also proved to be crucial during the alignment process, especially at grazing incidence, and was used in a complementary way to the optical microscope to accomplish this task. Indeed, selecting the Bi-Lα signal it is possible to obtain the desired sample orientation within a precision of about 1°, allowing for the detection and compensation of sample twist along the *a*-axis. XRD frames were collected using the FreLoN CCD detector mounted behind the sample when the fine adjustment (0.05° steps) of the rotation stage allowed for the appearance of the (0 0 *l*) equatorial series of Bragg reflections. An example of the XRD frames acquired with this procedure is reported in the Supporting Information, along with the sketch of the corresponding geometry and the details of the calibration performed with the Fit2d[22] software (see Figure S1).

The values of the *c*-axis lattice parameter have been determined from each XRD frame by performing a minimization procedure of the function describing the experimental positions of the (0 0 *l*) reflections, where the *c*-axis is the only fit parameter. The details concerning the calculation of this function are reported in the Supporting Information.

For fitting purposes, the uncertainties of the peak positions have been determined by considering, for each diffraction spot, the dispersion of its intensity in the *xz*-plane of the CCD camera as a Gaussian distribution; hence, the FWHM measured with Fit2d was divided by 2.35. On the other hand, the uncertainty of the *c*-axis value has several contributions. Apart from the one originating from the minimization process, additional non-negligible contributions come from the depth of focus of the optical microscope, from the uncertainty of the sample-to-detector

distance and the thickness of the crystals. All of them have been taken into account for the final estimation of the uncertainty of the *c*-axis value.

Following this procedure, it has been possible to retrieve information on both the structural and the electrical properties of Bi-2212 from the same crystals, at different doses of X-ray irradiation. To the best of our knowledge, such a data collection is unique in providing this combined information on the same single crystals.

At least two irradiation sessions were applied to each sample. To evaluate the absorbed X-rays dose *D*, the following formula was used:

$$D = \frac{\Phi_0 \ \Delta t \ E_0 \ \eta}{m_\Phi} = \frac{\Phi_0 \ \Delta t \ E_0 \ (1-e^{-\frac{t}{\lambda_a}})}{V_\Phi \rho_m} \quad , \qquad (1)$$

where Δt is the irradiation time and $\eta = 1 - e^{-\frac{t}{\lambda_a}}$ is the fraction of photons absorbed within the crystal, with t the thickness of the material crossed by the beam and λ_a = 17.38 μm the attenuation length in Bi-2212 for the incoming photons with energy E_0 = 17.05 keV.[23] Moreover, m_Φ in eq 1 represents the mass of the irradiated portion of the crystal, which corresponds to the volume V_Φ resulting from the crystal area illuminated during the XRF map acquisition multiplied by the thickness t of the crystal along the direction of the beam.

The results of the electrical characterization for one of the samples are summarized in Figure 2, where the *ab*-plane resistivity versus temperature behavior and the T_c variation versus the resistivity at 295 K are illustrated for the as-grown condition and after each of the three irradiation treatments. The results for the other sample are very similar and are shown in the Supporting Information for clarity (see Figure S2). Three main features can be observed: i) the presence of a double transition (Figure 2a and 2b), ii) a monotonous increase of T_c (Figure 2d and Table 1) and iii) of the normal state resistivity with increasing the dose (Figure 2a).

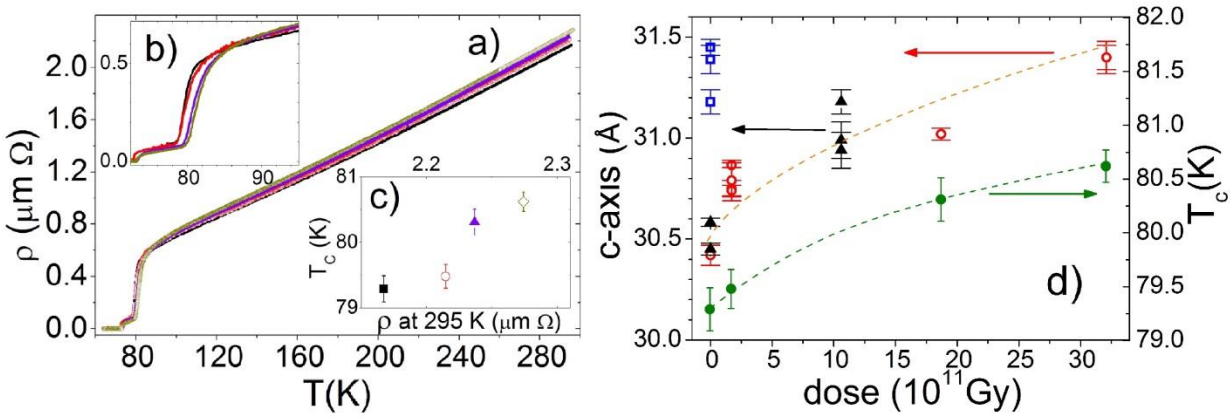

Figure 2. a) Four-probes *ab*-plane resistivity versus temperature curves corresponding to sample WBAP013 in as-grown conditions (black squares), after the first dose (red circles), the second dose (blue triangles) and the third one (green diamonds). b) Blow-up of Figure 2a corresponding to the transition region, where the curve crossover is visible. c) T_c versus resistivity at room temperature for each of the four experimental conditions. The resistivity values have been obtained via accurate geometrical SEM characterization, error bars on ρ are negligible on these scales and hence omitted. d) Dependence of the *c*-axis lattice parameter on the X-rays dose for both of the measured samples (WBAP013 - red circles, WBAP014 - black triangles). Blue squares refer to measurements of the crystal WBAP013 taken in a region under an Ag contact. The T_c vs dose behavior of the same crystal is also shown (green circles). The dashed lines represent just a guide to the eye.

The two transitions, clearly visible in the blow-up of Figure 2b, show the same relative position of the curves but are centered around two different temperatures, nearly 73 K and 80 K, respectively. They have different heights of the step, which implies different cumulative lengths for the corresponding crystal phases along the *a*-axis.[24,25] For these reasons, it is possible to state

that the latter transition corresponds to the main Bi-2212 crystallographic phase of the sample, while the former can be ascribed to another minor, oxygen-depleted phase. Based on previous observations,[26] it can be supposed that such a minor phase is brought about by silver ions diffusing from the electrical contacts into the top layers of the crystals during the annealing process. This issue will be further discussed in the following. On the other hand, the simultaneous appearance in the curves of the above-mentioned increase of T_c and of the normal state resistivity (see also Figure 2c) generates the presence of a crossover region located slightly above the transition, at approximately 85 K (Figure 2b).

D (10^{11}Gy)	T_c (K)	σ_{Tc} (K)	c_{avg} (Å)	σ_c (Å)
0	79.29	0.20	30.42	0.04
1.72	79.48	0.18	30.79	0.06
18.7	80.31	0.20	31.02	0.03
32.1	80.62	0.15	31.40	0.05

Table 1. Mid-point transition temperature T_c and average c-axis value c_{avg} as a function of the X-ray dose D for one of the samples (WBAP013).[i]

[i] The average of the c-axis values excludes the region under the electrical contacts. σ_{Tc} and σ_c represent the uncertainties of T_c and c_{avg}, respectively.

The increase of the resistivity with increasing the dose confirms some preliminary observations by our group.[27] Moreover, comparing Figure 2c with the typical behavior of Bi-2212 as a function of the oxygen doping[28] suggests that the crystals shift from the slightly over-doped regime corresponding to the as-grown condition towards an optimally-doped one with increasing the X-ray dose.

Figure 2d displays the behavior of the *c*-axis lattice parameter versus the dose for both samples and represents our main experimental result. The as-grown values averaged over different positions between the voltage contacts correspond to (30.42 ± 0.04) Å for sample WBAP013 and (30.517 ± 0.018) Å for sample WBAP014, respectively. These values are slightly lower (0.1 - 0.4%) and less precise than the measurements reported by previous studies,[29] even compared to our past experience on single crystals of the same material.[27] From this point of view, it should be pointed out that the technique adopted in the present work to determine the *c*-axis length is based on a quite limited number of reflections in comparison with single-crystal or powder-XRD experiments. Moreover, the approximation $\sin^2\theta \approx tg^2\theta$ used to predict the peak positions according to eq S.2 is likely responsible for our small systematic underestimation of the *c*-axis. Of course, this does not invalidate the general trend of our results, all the more so because the electric measurements do not show any trace of filamentary intergrowths of the $Bi_2Sr_2Ca_2Cu_3O_{10+\delta}$ (Bi-2223) phase,[24] which could affect the *c*-axis determination.

Therefore, it is possible to state from Figure 2d that an increase of the *c*-axis lattice parameter occurs as a consequence of irradiation, with the same trend for both samples and a maximum elongation of approximately 1 Å (i.e. ≈ 3%) at the highest dose. Since the *c*-axis value is closely related to the carrier density,[30] these results support the observation that X-rays can induce a shift from an over-doped state to an optimally doped one in Bi-2212. The decrease in the carrier

number density is about 5% for a dose of 3.21×10^{12} Gy, as determined from the *ab*-plane resistivity at room temperature. It is very likely that such a change in the doping state can also affect the Bi-2212 superstructure modulation in the *ab*-plane recently highlighted by Poccia *et al*.;[31] however, the investigation of this possible effect is beyond the scope of the present paper.

In principle, this phenomenon could be ascribed either to the out-diffusion of the interstitial oxygen or to the appearance of a mobility edge for the holes, possibly triggered by the X-rays through the generation of disorder in the interstitial oxygen superstructure.[32,33] Whatever the origin of the carrier decrease is, a displacement of the interstitial oxygen is involved, whose activation energy can be assumed as about 0.93 eV.[34]

This displacement could be caused by a knock-on process induced by the secondary electrons originating from the synchrotron radiation exposure of the sample[27], as also suggested by a study performed on micro-bridges of the $YBa_2Cu_3O_{7-x}$ (Y-123) superconductor[35]. Another possibility to be considered is represented by the local temperature increase induced by the final phonon-assisted decay of the power delivered to the crystals by the X-ray nano-beam. Indeed, this option is supported by several studies where some thermal treatment brings about an oxygen depletion or out-diffusion with consequent modifications of the electrical properties of the crystals.[27,29,36]

In order to assess the importance of the heating induced by the synchrotron radiation in the present experiment, we developed a 3D finite element model (FEM) using the commercial software COMSOL Multiphysics® to simulate the corresponding temperature field in the region between the voltage electrical contacts.

The model geometry and the details about the physical properties of the corresponding materials are described in Figure S3 and Table S1 of the Supporting Information. For simplicity, silver electrodes were not introduced in the model because their distance from the region of

interest (≈ 50 μm) is expected to induce negligible effects on the quality of the results. Two different simulations were performed for each sample, mimicking the experimental conditions of frontal and lateral incidence, i.e. with the beam impinging in the center of the *ab* and *ac* surfaces, respectively. These two cases have been taken as representative of the more general conditions of irradiation, where the beam hits the crystal surface in different positions during the raster scan of the irradiation process.

To simulate the temperature field, the heat equation has been computed considering both conduction and convection phenomena in steady state at the temperature of 300 K. The energy balance is expressed through the following partial differential equation:

$$\nabla \cdot \left(-k\nabla T\right) + \rho_m C_p \vec{u} \cdot \nabla T = Q, \tag{2}$$

where k is the thermal conductivity, T is the temperature, ρ_m the mass density per unit volume, C_p the heat capacity, $\vec{u}$ is the air velocity and Q the heat source. This last term represents the power per unit volume delivered to the crystal, calculated as the portion of energy absorbed from the beam and distributed in an approximately homogeneous way in the volume V obtained by the intersection of the incoming beam with the crystal:

$$Q = \frac{\Phi_0 E_0 \eta}{V} = \frac{P_{abs}}{V}, \tag{3}$$

where P_{abs} is the absorbed power. Eq 3 allows for retrieving the Q value necessary to solve the FEM, as reported in Table 2. Since the substrate volume is much greater than the crystal one, the reference temperature of 300 K has been set as a boundary condition on the bottom and side surfaces of the substrate.

configuration	t (μm)	η (%)	P_{abs} (μW)	V (μm^3)	Q (10^{15} Wm^{-3})
frontal	1.6	8.7	45	0.022	2.09
lateral	13.55	54.1	280	0.184	1.52

Table 2. Parameters used to determine the value of the volume power density Q in the FEM for both experimental configurations in the case of sample WBAP013.[ii]

The temperature distribution evaluated through the FEM is shown in Figure 3 for some representative cases. The condition of lateral incidence appears to be more effective from the point of view of the energy release, inducing a temperature increment of about 23.6 K, which is nearly four times larger than the frontal incidence case. However, in both cases the significance of the temperature increase is limited to a region centered at the beam position that is about 35 μm long in the *a*-axis direction, confirming that silver contacts could be safely neglected. Concerning the temperature distribution along the *c*-axis direction, it can be noticed that the maximum thickness of the region with some significant increase is always limited to about 20 μm in air, therefore confirming the validity of the assumption about the boundary conditions. Correspondingly, it is also possible to appreciate that the temperature is practically constant in this direction inside the crystal. Similar results have been obtained for the other sample.

[ii] t represents the thickness of the crystal in the direction of the beam, η is the fraction of absorbed photons, P_{abs} is the absorbed power, and V the interaction volume between the beam and the crystal

.

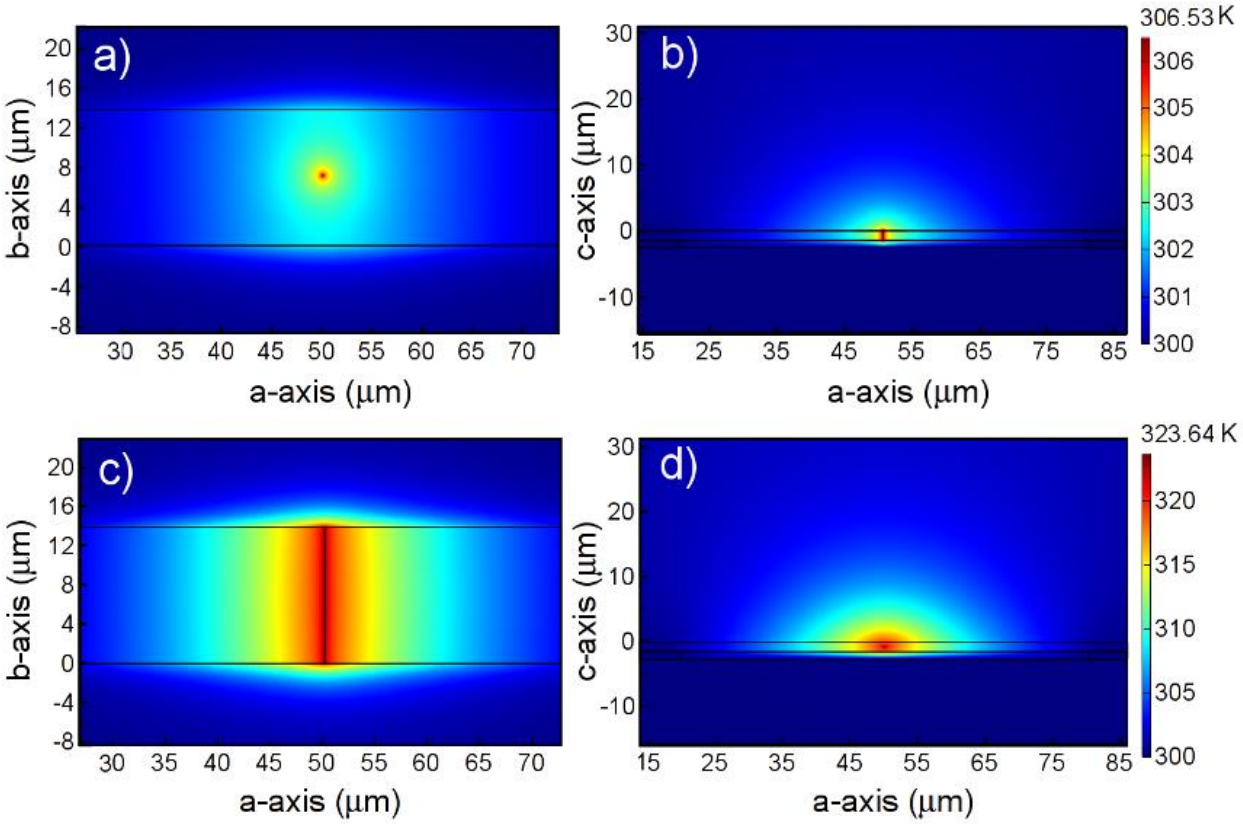

Figure 3. Temperature field induced by the synchrotron nano-beam on the sample WBAP013 according to FEM simulations in the region between the voltage electrodes, in different incidence geometries: (a) frontal incidence, section at half the thickness of the crystal; (b) frontal incidence, section at half the width of the crystal, passing through the center of the beam; (c) lateral incidence, section at half the thickness of the crystal, passing through the center of the beam; (d) lateral incidence, section at half the width of the crystal.

According to these simulation results, the temperature increase induced by the X-ray nano-beam is far too moderate to thermally activate the interstitial oxygen diffusion in Bi-2212, hence

we can eliminate radiation heating as the main source of the observed modifications. Thereby oxygen displacement is very likely due to 17 keV photon-induced secondary electrons.

Taking advantage of the nanometric spatial resolution, we have also collected XRD frames for one of the sample in pristine conditions in the region covered by a silver electrode, determining the corresponding *c*-axis values to investigate possible effects induced by the proximity of the metal-superconductor interface (Figure 2d, blue squares). Considering the average value under the silver contact (31.34 ± 0.13) Å in comparison with the average value (30.42 ± 0.04) Å between the contacts, a remarkable elongation of the *c*-axis of about 0.9 Å can be clearly identified. This information confirms our previous hypothesis about the origin of the double transition in Figure 2a and 2b. Indeed, since in Bi-2212 the length of the *c*-axis is monotonically related to the carrier density[29], this evidence clarifies that an oxygen-depleted phase actually exists under the voltage contacts, whose extension is of the order of 10 μm around them. Therefore, the oxygen withdrawal process[26] by the Ag electrodes must have taken place, very likely during the thermal treatment for contact preparation.

In conclusion, we investigated the effect of irradiation by a hard X-ray nano-beam on both the electrical and the structural properties of Bi-2212. The elongation of the *c*-axis with the dose provides direct evidence that irradiation induces a change in the doping level of the material from an over-doped state towards a progressively more under-doped one. This is also confirmed by the monotonic dependence of room-temperature resistivity and T_c. FEMs allowed us to rule out oxygen displacement due to a local heating induced by the irradiation and suggest the photon-induced oxygen atom displacement as the most likely source of the doping modifications. These results imply the possibility of turning superconducting oxides into insulating ones by increasing the X-ray dose, and therefore confirm the possibility for a direct-writing, photoresist-

free lithography to be developed for these materials, extending it from La_2CuO_{4+y}[16] to Bi-2212, more used for applications. This is particularly interesting in view of the forthcoming availability of ever more powerful and focused X-ray sources, like for instance XFELs. The fact that the mechanism for doping alteration seems to rely on secondary electrons implies that the expected ultimate resolution for this new kind of possible photolithography should be in the range of the photoelectron inelastic mean free path (i.e. about 10 nm), substantially confirming the estimation by Poccia *et al*.[16] The possibility of exceeding the present limits of the focused-electron-beam and of the focused-ion-beam lithography in terms of contamination, mechanical stability and 3D fabrication capability is expected to stimulate further research in this direction. Further investigation is also necessary to clarify the dynamics of the interstitial oxygen atoms under irradiation.

Finally, we have also proved the localization of the chemically-induced oxygen depletion caused in Bi-2212 by the proximity to metallic contacts, estimating its length scale for the conditions used in our sample preparation process. This result highlights how large the perturbation of both the superconducting properties and the crystal structure can be at the metal-oxide interface, requiring very careful treatment during the fabrication of micro- and nano-devices.

ASSOCIATED CONTENT

Supporting Information

Determination of the *c*-axis lattice parameter via XRD, electrical characteristics measured on another sample at different irradiation doses, and details of the 3D Finite Element Model. This material is available free of charge via the Internet at http://pubs.acs.org.

AUTHOR INFORMATION

Corresponding Author

*E-mail: marco.truccato@unito.it

ACKNOWLEDGMENTS

The authors thank the entire crew at ID22 for their support and Carmelo Prestipino for fruitful discussions. Technical support from Compagnia di San Paolo-Nanofacility Piemonte at INRiM is gratefully acknowledged. The work was partially funded by project ORTO11RRT5 of University of Torino.

REFERENCES

(1) Pease, R. F.; Chou S. Y. Lithography and other patterning techniques for future electronics *Proceedings of the IEEE* **2008**, 96, 248-270.

(2) Solak, H. H. Nanolithography with coherent extreme ultraviolet light *J. Phys. D: Appl. Phys.* **2006**, 39, R171-R188.

(3) Solak, H.H.; He, D.; Li, W.; Singh-Gasson, S.; Cerrina, F.; Sohn, B. H.; Yang, X. M.; Nealey, P. Exposure of 38 nm period grating patterns with extreme ultraviolet interferometric lithography *Appl. Phys. Lett.* **1999**, 75, 2328-2330.

(4) Bourdillon, A. J.; Boothroyd, C. B.; Williams, G. P.; Vladimirsky Y. Near field x-ray lithography simulations for printing fine bridges *J. Phys. D: Appl. Phys.* **2003**, 36, 2471–2482.

(5) Ehrfeld, W.; Lehr, H. Deep X-ray lithography for the production of 3-dimensional microstructures from metals, polymers and ceramics *Radiat. Phys. Chem.* **1995**, 45, 349-365.

(6) Ehrfeld, W.; Münchmeyer, D. Three-dimensional microfabrication using synchrotron radiation *Nuclear Instruments and Methods in Physics Research A* **1991**, 303, 523-531.

(7) Randolph, S. J.; Fowlkes, J. D.; Rack, P. D. Focused, nanoscale electron-beam-induced deposition and etching *Crit. Rev. Solid State Mat. Sci.* **2006**, 31, 55–89.

(8) Tseng, A. A. Recent developments in nanofabrication using Focused Ion Beams *Small* **2005**, 1, 924–939.

(9) Tseng, A. A.; Notargiacomo, A.; Chen, T. P. Nanofabrication by scanning probe microscope lithography: a review *J. Vac. Sci. Technol. B* **2005**, 23, 877-894.

(10) Katoha, T.; Nishi, N.; Fukagawa, M.; Ueno, H.; Sugiyama, S. Direct writing for three-dimensional microfabrication using synchrotron radiation etching *Sensors and Actuators A* **2001**, 89, 10-15.

(11) Costacurta, S.; Malfatti, L.;Patelli, A.; Falcaro, P.; Amenitsch, H.; Marmiroli, B.; Grenci, G.; Piccinini, M.; Innocenzi, P. Deep X-ray lithography for direct patterning of PECVD films *Plasma Process. Polym.* **2010**, 7, 459–465.

(12) Leontowich, A. F. G.; Hitchcock, A. P. Zone plate focused soft X-ray lithography *Appl. Phys. A* **2011**, 103, 1–11.

(13) Innocenzi, P.; Kidchob, T.; Costacurta, S.; Falcaro, P.; Marmiroli, B.; Cacho-Nerind, F.; Amenitsch, H. Patterning block copolymer thin films by deep X-ray lithography *Soft Matter* **2010**, 6, 3172–3176.

(14) Leontowich, A. F. G.; Hitchcock A. P.; Watts, B.; Raabe, J. Sub-25 nm direct write (maskless) X-ray nanolithography *Microelectronic Engineering* **2013**, 108, 5-7.

(15) Larciprete, R.; Gregoratti, L.; Danailov, M.; Montereali, R. M.; Bonfigli, F.; Kiskinova M. Direct writing of fluorescent patterns on LiF films by x-ray microprobe *Appl. Phys. Lett.* **2002**, 80, 3862-3864.

(16) Poccia, N.; Fratini, M.; Ricci, A.; Campi, G.; Barba, L.; Vittorini-Orgeas, A.; Bianconi, G.; Aeppli, G.; Bianconi, A. Evolution and control of oxygen order in a cuprate superconductor *Nature materials* **2011**, 10, 733-736.

(17) Ozyuzer, L.; Koshelev, A. E.; Kurter, C.; Gopalsami, N.; Li, Q.; Tachiki, M.; Kadowaki, K.; Yamamoto, T.; Minami, H.; Yamaguchi, H.; Tachiki, T.; Gray, K. E.; Kwok, W.-K.; Welp, U. Emission of Coherent THz Radiation from Superconductors *Science* **2007**, 318, 1291-1293.

(18) Ozyuzer, L.; Simsek, Y.; Koseoglu, H.; Turkoglu, F.; Kurter, C.; Welp, U.; Koshelev, A. E.; Gray, K. E.; Kwok, W. K.; Yamamoto, T.; Kadowaki, K.; Koval, Y.; Wang, H. B.; Müller, P. Terahertz wave emission from intrinsic Josephson junctions in high-T_C superconductors *Supercond. Sci. Technol.* **2009**, 22, 114009.

(19) Benseman, T. M.;Koshelev, A. E.; Kwok, W.-K.; Welp, U.; Vlasko-Vlasov, V. K.; Kadowaki, K.; Minami, H.; Watanabe, C.; Direct imaging of hot spots in $Bi_2Sr_2CaCu_2O_{8+\delta}$ mesa terahertz sources *J. Appl. Phys.* **2013**, 113, 133902.

(20) Latyshev Yu, I.; Gorlova, I.; Nikitina, A. M.; Antonkhina, S. G.; Zybtsev, S. G.; Kukhta, N. P. Growth and study of single-phase 2212 BSCCO whiskers of submicron cross-sectional area *Physica C* **1993**, 216, 471-477.

(21) Khan, M. M. R.; Cagliero, S.; Agostino, A.; Beagum, M.; Plapcianu, C.; Truccato, M; Control of the oxygen doping in Bi-2212 whiskers by means of their synthesis process *Supercond. Sci. Technol.* **2009**, 22, 085011.

(22) http://www.esrf.eu/computing/scientific/FIT2D/FIT2D_REF/fit2d_r.html.

(23) The attenuation length λ_a for Bi-2212 has been obtained from the Center for X-Ray Optics at LBNL website: http://henke.lbl.gov/optical_constants/atten2.html.

(24) Truccato, M.; Imbraguglio, D.; Agostino, A.; Cagliero, S.; Pagliero, A.; Motzkau, H.; Rydh, A. Photoconductivity effects in mixed-phase BSCCO whiskers *Supercond. Sci Technol.* **2012**, 25, 105010.

(25) Truccato, M.; Cagliero, S.; Agostino, A.; Panetta, M.; Rinaudo, G. Electrical study of an unusual phase transformation in a $Bi_2Sr_2Ca_2Cu_3O_{10+x}$ whisker at room temperature *Supercond. Sci. Technol.* **2006**, 19, 1003-1009.

(26) Luo, Y. S.; Yang, Y.-N.; Weaver, J. H. Mechanism for adatom-induced disruption of $Bi_2Sr_2CaCu_2O_8$ (001): Scanning-tunneling-microscopy studies of Ag-, Au-, and Cr-overlayer growth Phys. Rev. B **1992**, 46, 1114-1121.

(27) Aldica, G.; Cagliero, S.; Agostino, A.; Lamberti, C.; Truccato, M. 17 keV photon induced damage of Bi-2212 whiskers by synchrotron μ-beam exposure *Supercond. Sci. Technol.* **2011**, 24, 035009.

(28) Watanabe, T.; Fujii, T.; Matsuda, A. Anisotropic resistivities of precisely oxygen controlled single-crystal $Bi_2Sr_2CaCu_2O_{8+\delta}$: systematic study on "Spin Gap" effect *Phys. Rev. Lett.* **1997**, 79, 2113-2116.

(29) Inomata, K.; Kawae, T.; Nakajima, K.; Kim, S. J.; Yamashita, T. Junction parameter control of $Bi_2Sr_2CaCu_2O_{8+\delta}$ stacked junctions by annealing *Appl. Phys. Lett.* **2003**, 82, 769-771.

(30) Chen, X. H.; Yu, M.; Ruan, K. Q.; Li, S. Y.; Gui, Z.; Zhang, G. C.; Cao, L. Z. Anisotropic resistivities of single-crystal $Bi_2Sr_2CaCu_2O_{8+\delta}$ with different oxygen content Phys. Rev. B **1998**, 58, 14219-14222.

(31) Poccia, N.; Campi, G.; Fratini, M.; Ricci, A.; Saini, N. L.; Bianconi, A. Spatial inhomogeneity and planar symmetry breaking of the lattice incommensurate supermodulation in the high-temperature superconductor $Bi_2Sr_2CaCu_2O_{8+y}$ Phys. Rev. B **2011**, 84, 100504.

(32) Ishibashi, T.; Yoda, O.; Goda, S. Gamma-ray irradiation effects of as-grown Bi–Sr–Ca–Cu–O thin-films on the superconducting property and modulation periodicity. *Physica C* **1994**, 228, 379-382.

(33) Aldica, G.; Vasiliu, F.; Geru, I. I.; Puscasu, B. M. The effect of electron beam irradiation on electron diffraction patterns of Bi–Sr–Ca–Cu–O high-Tc superconductors. *J. Supercond.* **2000**, 13, 623–631.

(34) Runde, M.; Routbort, J. L.; Rothman, S. J.; Goretta, K. C.; Mundy, J. N.; Xu, X.; Baker, J. E. Tracer diffusion of oxygen in $Bi_2Sr_2CaCu_2O_{8+\delta}$ *Phys. Rev. B* **1992**, 45, 7375-7382.

(35) Tolpygo, S. K.; Lin, J.-Y.; Gurvitch, M.; Hou, S. Y.; Phillips, M. Effect of oxygen defects on transport properties and T_c of $YBa_2Cu_3O_{6+x}$: displacement energy for plane and chain oxygen and implications for irradiation-induced resistivity and T_c suppression *Phys. Rev. B* **1996**, 53, 12462-12474.

(36) Cagliero, S.; Piovano, A.; Lamberti, C; Khan, M. M.; Agostino, A.; Gianolio, D.; Mino, L.; Sans, J. A.; Manfredotti, C.; Truccato, M. Synchrotron study of oxygen depletion in a Bi-2212 whisker annealed at 363 K *J. Synchrotron Rad.* **2009**, 16, 813-817.

GRAPHICAL ABSTRACT